Supporting information for

Characterization of a High-Spin Nonheme Fe^{III}–OOH Intermediate and Its Quantitative Conversion to an Fe^{IV}=O Complex

Feifei Li,[1] Katlyn K. Meier,[2] Matthew A. Cranswick,[1]
Mrinmoy Chakrabarti,[2] Katherine M. Van Heuvelen,[1] Eckard Münck,[2,*]
and Lawrence Que, Jr.[1,*]

(1) Department of Chemistry and Center for Metals in Biocatalysis, University of Minnesota, Minneapolis, MN 55455

(2) Department of Chemistry, Carnegie Mellon University, Pittsburgh, PA 15213

Materials and Syntheses.

All reagents including the 1,4,8,11-tetramethyl-1,4,8,11-tetraazacyclotetradecane (TMC) ligand, H_2O_2 (30 wt. % in H_2O) and anhydrous grade acetonitrile (99.5%) were purchased from commercial sources such as Sigma-Aldrich and Fisher Chemical and used as received unless otherwise noted. $H_2{}^{18}O_2$ (10 wt. % in H_2O; 90% ^{18}O incorporation), D_2O_2 (30 wt. % in D_2O; 98% D), and DClO4 (68%. in D_2O, 99% D) for resonance Raman sample preparation were purchased from ICON Isotopes or Sigma-Aldrich. $Fe^{II}(TMC)(CH_3CN)(OTf)_2$ was prepared by literature methods in a nitrogen-filled glove-box.[1] The concentrations of H_2O_2 were confirmed by ^1H NMR in CD_3CN as solvent.[2] For kinetic experiments, commercially available 30 wt. % H_2O_2 in H_2O (~10 M) and 11.5 M $HClO_4$ in H_2O were diluted to 1 M and 1.15 M with CH_3CN prior to use, respectively. Solutions of **2** used for proton dependence analysis and the Eyring plot were typically obtained by treating ~2.0 mM $[Fe^{II}(TMC)(CH_3CN)]^{2+}$ in 1.5 mL CH_3CN with 10 equiv. NEt_3 (e.g. 60 µl of a 0.5-M solution) followed by 20 equiv. H_2O_2 (e.g. 60 µl of a 1-M solution) in CH_3CN at –40 °C. Aliquots of a 1.15-M $HClO_4$ solution were then added to these solutions without removing the excess NEt_3 and H_2O_2.

Physical Methods.

UV-Vis spectra were recorded on a HP8453A diode-array spectrometer equipped with a cryostat from Unisoku Scientific Instruments (Osaka, Japan) for temperature control.

Mössbauer spectra were recorded with two spectrometers, using Janis Research Super-Varitemp dewars that allowed studies in applied magnetic fields up to 8.0 T in the temperature range from 1.5 to 200 K. Mössbauer spectral simulations were performed using the WMOSS software package v2.5 (WEB Research, Edina, MN) as well as a modified version of SPHMOSS.[3] Isomer shifts are quoted relative to Fe metal at 298 K. X-band EPR spectra were obtained on a Bruker Elexsys E-500 spectrometer equipped with an Oxford ESR-910 cryostat. EPR spectral simulations were carried out using a Windows software package (SpinCount v3.1.2) available from Professor Michael Hendrich of Carnegie Mellon University.

Fe K-edge XAS data were collected for frozen solution samples of **1** and **2** at beamline 7-3 of the Stanford Synchrotron Radiation Lightsource (SLAC National Accelerator Laboratory, Menlo Park, CA). The data were collected in fluorescence mode using a 30-element germanium detector (Canberra) at a sample temperature of *ca.* 10 K over the energy range of 6.9–8.0 keV, as previously described.[4] Nine total scans were collected at a single sample spot for **1**, while nine total scans at three different sample spots were obtained for **2**. The raw XAS data were examined, averaged, and processed for analysis with EXAFSPAK.[5] The energies were referenced against an internal Fe foil reference at 7112.0 eV. No deglitching was carried out, nor were any points deleted from the raw XAS data. A unit-weighted average was used for both data sets. For both **1** and **2**, 17 out of 30 detector elements were included in the average. Individual scans were examined for photoreduction; no evidence of photoreduction was found for either sample based on the lack of changes in either edge energy or pre-edge intensity. The $k^3\chi(k)$ EXAFS data was analyzed using EXAFSPAK with phase and amplitude parameters obtained from FEFF 8.40.[6] The goodness-of-fit parameter F defined as $\Sigma(\chi_{calcd} - \chi_{expt})^2$. A second goodness-of-fit parameter F' is defined as $F' = F^2 / \nu$, where $\nu = N_{IDP} - \rho$. N_{IDP} is the number of independent data points ($N_{IDP} = 2\Delta k \Delta r/\pi$), while ρ is the number of floated variables in each optimization step.[7] F' is a measure of whether an added shell significantly improves the fit. In all analyses, the coordination number of a given shell was a fixed parameter, and was varied iteratively while bond lengths and Debye-Waller factors were allowed to freely float. The amplitude reduction factor S_0 was fixed at 0.9, while the edge shift parameter E_0 was allowed to float but was constrained to a common value for all shells. Thus in any given fit, ρ = (2 × number of shells) + 1.

Resonance Raman spectra were collected on an ACTON AM-506M3 monochromator with a Princeton LN/CCD data collection system (LN-1100PB) using a Spectra Physics Model 2060 krypton laser or a Spectra Physics Beamlok 2065-7S argon laser, and Kaiser Optical holographic super-notch filters. Low-temperature spectra of **1** and **2** in CH_3CN were obtained at 77 K using a 135° backscattering geometry. Samples were frozen onto a gold-plated copper cold finger in thermal contact with a Dewar flask containing liquid nitrogen. The Raman frequencies were referenced to indene. Slits were set for a band-

pass of 4 cm^{-1} for all spectra. Raman spectra were baseline corrected, and intensity corrected to the 773 cm^{-1} solvent peak.

Progress of the conversion of $[Fe^{III}(TMC)(OOH)]^{2+}$ (**2**) to $[Fe^{IV}(O)(TMC)(CH_3CN)]^{2+}$ (**3**) was followed by monitoring the changes in absorbance at 500 nm for the decay of **2** and at 820 nm for the formation of **3**.[1] Reactions were monitored for more than six half lives. Fitting plots of reaction progress (absorbance at 500 nm and 820 nm) against time with typical first-order rate equations gave good fits and allowed the determination of observed rate constants for the decay of **2** and for the formation of **3** (k_{obs}). Errors associated with reaction rates were determined from at least three independent trials. Second order rate constants (k_2) were extracted from the linear plots of k_{obs} vs. [$HClO_4$]. Linear fits were obtained by using the *Fit Linear* function in Origin v8.07773. Activation parameters were extracted from a standard Eyring plot.

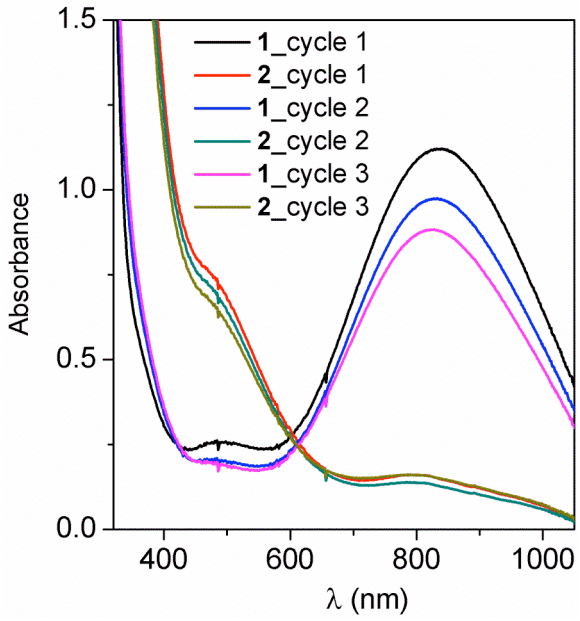

Figure S1. The interconversion between **1** and **2** upon addition of 15 equiv. $HClO_4$ or 15 equiv. NEt_3 in CH_3CN at –40 ºC. b = 1 cm. The concentration of **1** or **2** decreased by a factor of 0.93 between adjacent cycles due to the addition of aliquots of $HClO_4$ and NEt_3. Considering the dilution effect, the recovery yield is >95% between adjacent cycles.

Comments on the Mössbauer and EPR spectra

Side-on peroxo complex **1**

We have analyzed the Mössbauer spectra of **1** and **2** with the Hamiltonian

$$\mathcal{H} = D(S_z^2 - 35/4) + E(S_x^2 - S_y^2) + \mathcal{H}_{4th} + \beta \boldsymbol{S}\cdot\boldsymbol{g}\cdot\boldsymbol{B} + \boldsymbol{S}\cdot\boldsymbol{A}\cdot\boldsymbol{I} - g_n\beta_n\boldsymbol{B}\cdot\boldsymbol{I} + \mathcal{H}_Q \quad (1)$$

with

$$H_{4th} = \frac{F}{180}[35S_z^4 - 30S(S+1)S_z^2 + 25S_z^2 - 6S(S+1) - 3S^2(S+1)^2] + \frac{a}{6}[S_x^4 + S_y^4 + S_z^4 - \frac{1}{5}S(S+1)(3S^2+3S-1)] \quad (2)$$

Figure S2 shows two Mössbauer spectra of **1**. The 1.7 K spectrum originates from the ground Kramers doublet ($g_z \approx 9.8$, g_x, $g_y < 1$) of **2**. The magnetic splitting of the 6-line pattern is solely determined by *E/D* and A_z.[8] While the fourth-order terms, *a* and *F*, strongly affect the properties of the middle Kramers doublet, their effects on the properties of the ground and upper Kramers doublets are negligible. The Mössbauer spectrum of the ground doublet yields the z component of the electric field gradient (EFG) tensor; the y-component is obtained at 10 K from the upper Kramers doublet (this doublet also yields a 6-line pattern; the second line from the left in Figure S2B originates from the upper doublet and the associated high-energy line coincides with the high-energy line of the ground doublet). As the EFG tensor is traceless, all principal components are now known.

It can be seen that the 1.7 K spectrum has broad unresolved background absorption. This feature, representing roughly 30 % of the Fe, is also present in the low-field 4.2 K and 10 K spectra. Yet, for applied fields ≥ 3.0 T (Figure S3A-C) there is no evidence of a second species. The high field data show that this broad feature **must** belong to **1**. At first sight one might suspect that the shoulder at the low energy band in Figure 2A reflects the presence of a second species. However, analysis of the progression of spectra obtained with applied fields of 3.0, 4.0 and 8.0 T shows that the shoulder comes about as follows: At low field, Figure S2, the magnetic hyperfine field of the ground doublet is along z, as the expectation value of **S** along z, $\langle S_z \rangle$, is large and $\langle S_x \rangle$ and $\langle S_y \rangle$ are small ($\langle S_i \rangle = g_i/4$). For increasing applied magnetic field $\langle S_x \rangle$ and $\langle S_y \rangle$ increase and the

magnetic hyperfine field becomes more isotropic, following the applied field (for B > 3.0 T only the spin-down level of the ground doublet is appreciably populated at 4.2 K). The shoulder on the low energy feature arises from molecules for which the hyperfine field is close to the xy plane. The intensity of the shoulder increases with increasing applied field, as <**S**> becomes more isotropic. We suspect that the broad feature in Figure S2 represents an aggregated subpopulation of **1**. Aggregation would give rise to spin-dipolar interactions that could broaden the low field spectra but would be decoupled (i. e. suppressed) at B > 3.0 T. The EPR spectrum of **1** indicates the presence of only one species but, interestingly, our spin quantification accounts only for about 66 % of the iron (1.04 mM spin/1.56 mM Fe). This "missing" fraction is in accord with the Mössbauer data, suggesting that the iron contained in the broad species does not contribute an EPR signal in X-band. We have observed partial aggregation in other projects. Sometimes the problem can be overcome by dilution. However, **1** became unstable upon 10-fold dilution.

We have indicated in the caption of Figure S2 that we have distributed A_z to account for the line width. The slightly broadened lines of the 1.7 K spectrum could be accounted for by distributing *E/D* (relaxation can be excluded as the spin system of **1** is in the slow relaxation limit even at 120 K). However, the 8.0 T spectrum requires the distribution of some quantity, and as this spectrum does not depend on zero field splitting parameters (the electronic Zeeman term dominates), only a distribution of the components of the A-tensor can produce the desired broadening. Since distributing A_z produces the correct broadening both at 8.0 T and 50 mT, we have distributed this quantity, rather than all three components of **A**, using $\sigma_z/A_z = 0.02$. In order to obtain the right splitting for the 1.7 K/50 mT and 4.2K/8.0 T spectra we had to use an average $A_z/g_n\beta_n$ = -20.9 T and *E/D* = 0.28 ± 0.01.

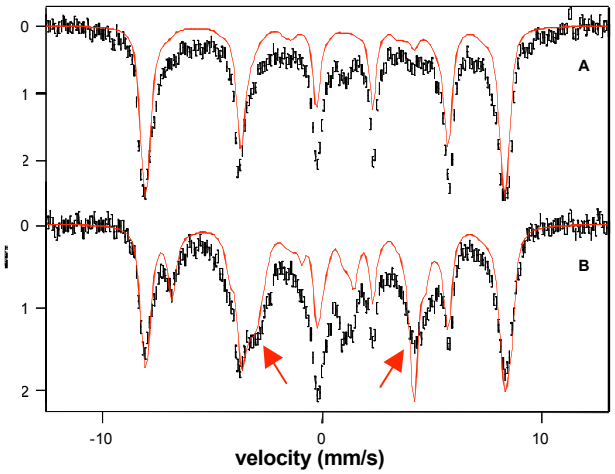

Figure S2. Mössbauer spectra of **1** in 3:1 PrCN/MeCN (black lines) recorded in magnetic fields applied parallel to the γ–rays at (A) 1.7 K and 50 mT; (B) 12K and 50 mT. The red lines are spectral simulations based on eqs S1 and S2, using D = –0.91 cm^{-1}, E/D = 0.27, a = –0.017 cm^{-1}, F = –0.108 cm^{-1}, $A_x/g_n\beta_n$ = –19.7 T, $A_y/g_n\beta_n$= –20.2 T and $A_z/g_n\beta_n$ = –20.9 T, ΔE_Q = –0.92 mm/s, η = 0.47, δ = 0.58 mm/s. In all simulations we have used a Gaussian distribution of A_z with σ_z/A_z = 0.02. The arrows in (B) point to the outermost features of the spectrum associated with the middle Kramers doublet.

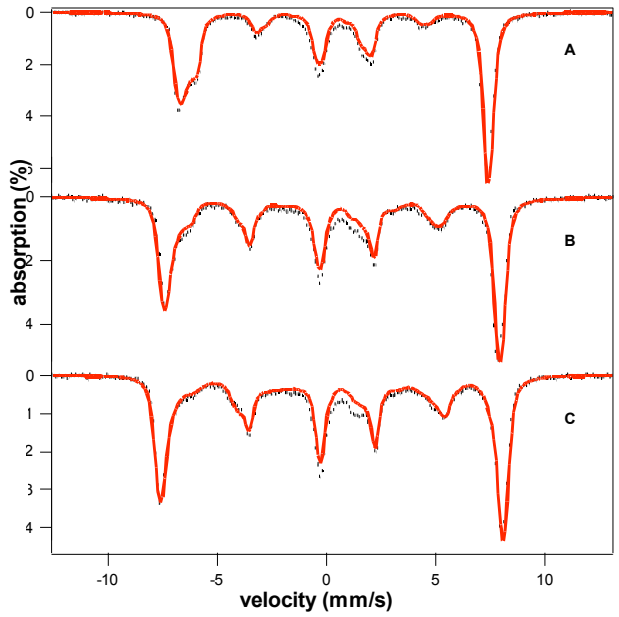

Figure S3. Mössbauer spectra of **1** recorded at 4.2 K in applied fields of 8.0 T (A), 4.0 T (B) and 3.0 T (C). The red lines are spectral simulations using the parameters quoted in Table S1.

We next comment on the EPR spectrum associated with the middle Kramers doublet of **1**. Figure S4 shows an expanded view of the spectrum of Figure 2C (black line) of the main text, and Figure S5 shows a plot of the effective g-values of the middle Kramers doublet as a function of *E/D* without inclusion of fourth-order terms. The horizontal lines, approximately, mark the experimental g_{eff}-values. In order to match the experimental *g*-values one could increase the intrinsic *g*-values to $g_x = 2.06$, $g_y = 2.01$ and $g_z = 2.04$, thus using a g_x value which seems unreasonably high. However, use of these g-values would not solve the problem as we require slopes $dg_{eff}/d\sigma_{E/D}$ that severely broaden $g_{eff,x}$ and $g_{eff,y}$ but keep the feature at $g_{eff,z}$ fairly sharp; see below. We therefore have added the fourth order terms.

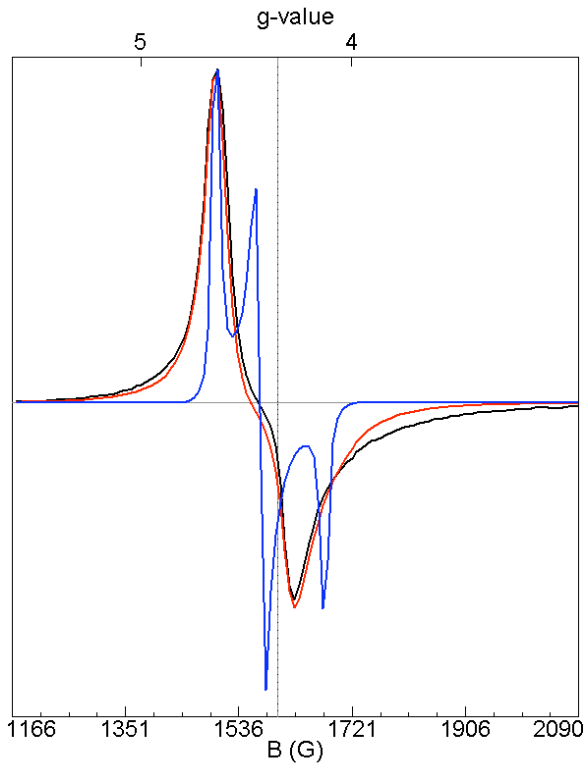

Figure S4. Expanded view of the EPR spectrum (black) of Figure 2C of the main text. The red line is the spectral simulation given in the main text. The blue line is a simulation for $\sigma_{E/D} = 0$ and a smaller packet line width.

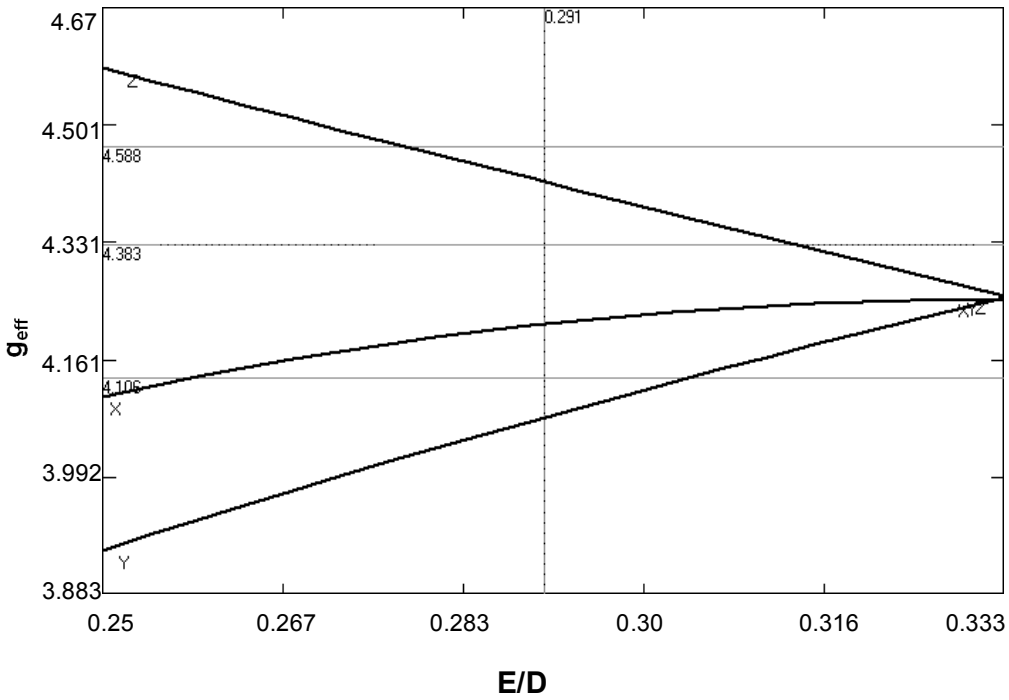

Figure S5. Effective *g*-values for the middle Kramers doublet of an $S = 5/2$ system as a function of E/D in the limit $\beta B/|D| << 1$ for $g_x = g_y = g_z = 2.00$. The horizontal lines indicate the "experimental" *g*-values; the vertical line indicates the E/D value of complex **1**, see text.

It should be pointed out that there will not be a unique solution to fit the spectrum of Figure S4, because the effective g-values of the middle Kramers doublet depend on E/D, a, F, g_x, g_y, g_z and to some extent on D. Unfortunately, the Mössbauer spectrum of the middle Kramers doublet is broadened by distributed parameters (at least A_z and E/D, and possibly A_x, A_y, and F). If the broadening were minor, as in the Mössbauer spectra of Fe superoxide dismutase-azide,[9] we could determine a and F from the Mössbauer spectra. We have explored the parameter space of a and F and found solutions for typical small a-values of $-(0.01 - 0.02)$ and $F = -(0.10 - 0.16)$ cm^{-1}, the particular value for F depending on how much one allows $\boldsymbol{g}$ to deviate from 2.00. Figure S6 shows a plot of the effective *g*-values versus E/D for $F = -0.108$ cm^{-1}; for other parameters see caption. This value of F not only produces the right g_{eff}, it also produces slopes $dg_{eff}/d(E/D)$ that broaden the resonances in a desirable way when E/D is distributed: thus, $g_{eff,x}$ remains quite sharp (the experimental feature at $g_{eff} = 4.58$) while $g_{eff,y}$ and $g_{eff,z}$ broaden significantly.

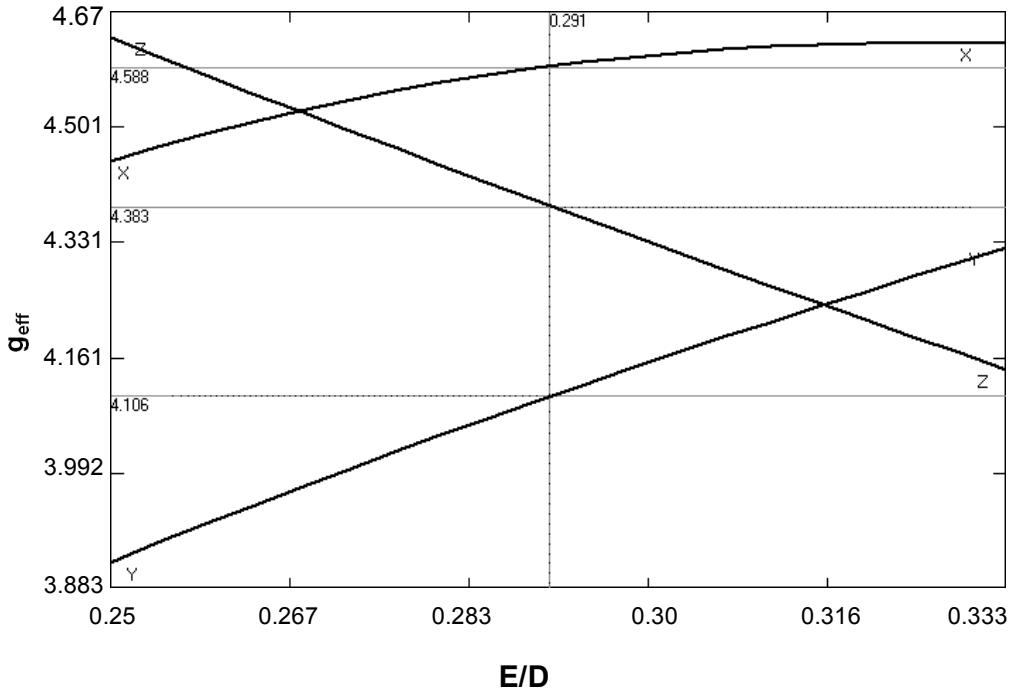

Figure S6. Effective *g*-values for the middle Kramers doublet for $F = -0.108$ cm^{-1}, $a = -0.017$ cm^{-1} and $\boldsymbol{g}$ = (2.04, 1.98, 2.03) versus *E/D*, calculated for B = 0.15 T. The horizontal lines indicate the "experimental" *g*-values; the vertical line indicates *E/D* value of complex **1**, see text.

A comparison of spectra simulated with and without $\sigma_{E/D}$ in Figure S4 illustrates how the experimentally observed trough at $g = 4.23$ arises, namely by merging of the negative portion of the derivative feature at $g_{eff} = 4.39$ with the negative "absorption-type" feature at $g_{eff} = 4.11$ through broadening by $\sigma_{E/D}$ (The trough does not correspond to a principal direction of $\boldsymbol{g}_{eff}$). We have also obtained acceptable fits by increasing F to -0.130 cm^{-1}, which allows one to keep the *g*-values a bit closer to $g = 2.00$ (2.02, 2.00, 2.02). By allowing $g_x = 2.05$ we found a solution for $F = -0.08$ cm^{-1} and $a = -0.07$ cm^{-1}. One can trade *g*-values for *F*- and *a*- values, but it is nevertheless apparent that a substantial *F*-term is required to explain the shape of the EPR feature. What gives rise to the large fourth-order terms will be the subject of future studies. Perhaps, mixing of the $S = 3/2$ states into the ground sextet (a Maltempo model in low symmetry) yields a mixed-spin state for which eq 1 is to be treated as an effective Hamiltonian.

One of the reviewers suggested to show, for the benefit of the reader, a "best" fit of the EPR spectrum without using the quartic terms; a least squares fit is shown in Figure S7. Despite the use of six free parameters the fit is inferior to the one obtained by

inclusion of quartic terms. Worst, in order to get the proper width, the fit requires that g_y is distributed by σ_{gy} =0.06, implying g_y values above and below g = 2.00, which is quite implausible in any model.

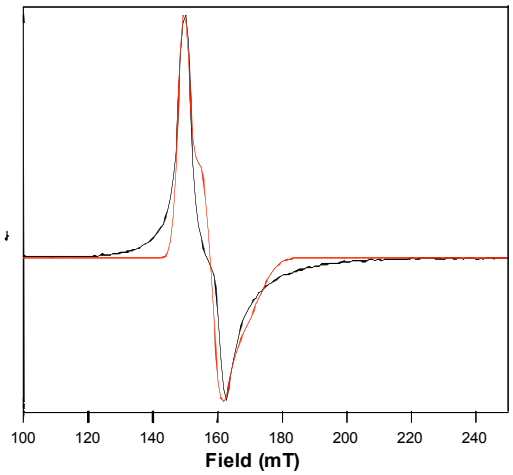

Figure S7. Simulation of the EPR signal of **1** (black) without inclusion of fourth-order terms (red line), where the black line represents the experimentally observed spectrum. For the simulation we fixed E/D = 0.29 as obtained from the Mössbauer data. The g-values were treated as free parameters and each of the three g-values was allowed to be distributed on a Gaussian of width σ_g. The best fit yielded g_x =2.06, g_y =2.01 g_z =2.04, σ_{gx}=0.03, σ_{gy} =0.06 and σ_{gz} = 0.02.

The arrows in the 12 K Mössbauer spectrum of Figure S2B mark the major absorption features associated with the middle Kramers doublet (The reader may keep in mind the presence of the above-mentioned background). With some additional broadening, perhaps by distributing F, the high energy feature could be broadened sufficiently to fit the data (without affecting the spectra of the ground and upper doublet).

Hydroperoxo complex **2**

The D and E/D parameters of complex **2** are such that the Mössbauer and EPR spectra would be quite insensitive to fourth-order terms. In fact, the Mössbauer and EPR spectra of **2** are quite 'normal'. The 8.0 T spectrum shown in Figure S8 is well simulated with the parameters of Table S1. For the simulations shown we have distributed A_y using σ_{Ay}/A_y = 0.05. The EPR spectrum of Figure 2D is well represented by the simulations. The simulations do not account for some of the absorption between the two low field

peaks. This absorption might be captured by using asymmetric distributions of *E/D*, but since the transition probability steeply rises as *E/D* decreases, the absorption not represented by the simulation likely represents only a minor fraction of the molecules. Mössbauer samples trapped for **2** contain at least 80% **2** and ~10% of **3** ($\Delta E_Q \approx 1.4$ mm/s and $\delta \approx 0.20$ mms/s).

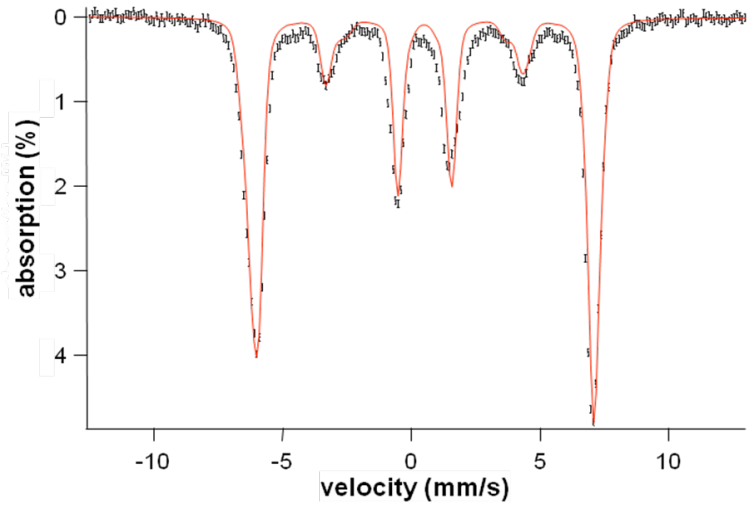

Figure S8. 4.2 K Mössbauer spectrum of **2** in 3:1 PrCN/MeCN recorded in a parallel field of 8.0 T (black line) and its simulation (red line). We have removed features belonging to 10% of **3** from the data; see Figure S9 for Mössbauer spectra of **3**.

Table S1. Spectroscopic properties of **1** and **2**.

	λ_{max}, nm (ε, $M^{-1}cm^{-1}$)	ν(O–O), cm^{-1} ($\Delta^{18}O$)	ν(Fe–O), cm^{-1} ($\Delta^{18}O$)	δ, mm/s	ΔE_Q, mm/s	*E/D*	*D*, cm^{-1}	$A_{iso}/g_n\beta_n$,T	η	*r*(Fe–O), Å	*r*(Fe–N), Å
1	835 (650)	826 (-41)	493 (-15)	0.58	–0.92	0.28	–0.91	–20.3	0.47	1.93	2.20
2	500 (450)	870 (-50)	676 (-24)	0.51	0.2[a]	0.097	2.5	–20.0	1.0[a]	1.92	2.15

[a] The EFG tensor of **2** is rhombic, $\eta = 1$, and 90° degrees rotated relative to the ZFS tensor, $\beta_{EFG} = 90$ in WMOSS. In the x,y,z frame of the zero-field splitting tensor, $V_{zz} = 0$, $V_{xx} = -V_{yy} > 0$.

Mössbauer spectra of Fe^{IV}=O complex **3**

Figure S9 shows 4.2 K Mössbauer spectra obtained after freezing a sample 5 min after **2** was allowed to decay in CH_3CN at –40 °C (See Figure 4 left panel for a plot of reaction trajectory). The zero field spectrum (bottom) is dominated by a quadrupole doublet with ΔE_Q = 1.40 mm/s and δ = 0.18 mm/s, representing Fe^{IV}=O complex **3**. The 7.5 T spectrum (top) exhibits a high-spin ferric species, outlined by the blue line above the data that represent 6-8 % of the Fe in the sample. The high-spin ferric species differs from **2**, suggesting **2** has completely decayed; the new ferric species represents perhaps some ferric decay product. (N.B: At 7.5 T only the M_S = -5/2 level of the S = 5/2 system is populated at 4.2 K. In zero field the six sublevels of the ground sextet are populated, spreading the absorption, with reduced amplitude.)

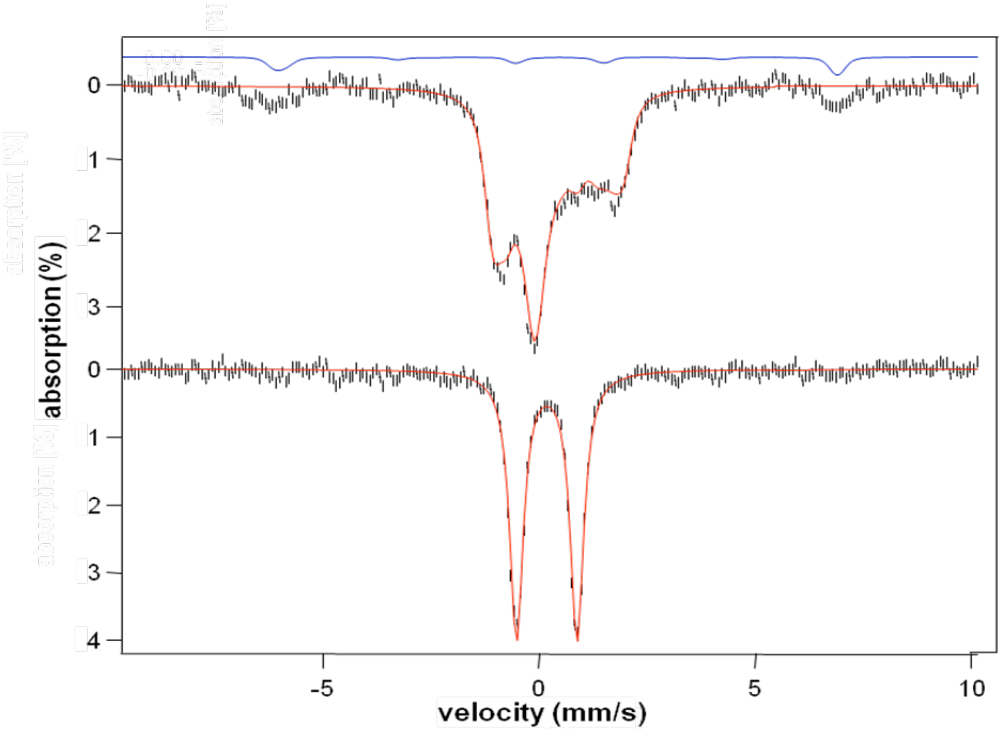

Figure S9. 4.2 K Mössbauer spectra of a sample frozen after the nascent **2** in CH_3CN was allowed to decay for 5 minutes and formation of **3** had been completed (see Figure 4 left panel for a plot of the reaction trajectory); spectra were collected at 7.5 T (top) and 0 T (bottom). A high-spin ferric contaminant (6-8% of Fe) is indicated by the blue line. The red lines are spectral simulations of **3** (drawn to represent 90% of Fe) using an S = 1 spin Hamiltonian with D = 27 cm^{-1}, E/D = 0, g = 2.0, $A_x/g_n\beta_n$ = -26 T, $A_y/g_n\beta_n$ = -19 T, $A_z/g_n\beta_n$ = -4 T, ΔE_Q = +1.40 mm/s, η = 0.5, δ = 0.18 mm/s.

Table S2. EXAFS fits for $[Fe^{III}(TMC)(\eta^2\text{–}O_2)]^+$ (**1**).[a]

	Fe–N/O			Fe–N/O			Fe•••C				
fit	*n*	*r*	σ^2	*n*	*r*	σ^2	*n*	*r*	σ^2	*F* [b]	*F'* [b]
1	6	2.21	40.4							425.5	9353
2	5	2.21	32.9							427.5	9442
3	4	2.23	3.0							341.3	6018
4	4	2.21	3.6	2	1.94	1.7				92.64	494.4
5	5	2.22	6.9	1	1.94	-1.4				149.2	1282
6	4	2.22	4.4	1	1.94	-1.1				118.1	803.6
7	5	2.21	5.4	2	1.93	1.3				117.0	788.7
8	4	2.21	3.5	2	1.94	1.7	4	3.07	8.4	60.34	237.1
9	**4**	**2.20**	**3.2**	**2**	**1.93**	**2.5**	**4**	**2.98**	**2.5**	**27.58**	**56.95**
							4	**3.13**	**2.7**		

[a] Fourier transform range k = 2.0 –15.0 Å^{-1} (resolution = 0.12 Å). r is in units of Å; σ^2 is in units of 10^{-3} Å^2. All fits shown here were to Fourier-filtered data employing a back transformation range of 0.3-3.0 Å. Bolded fit parameters represent the best fit.

[b] Goodness-of-fit parameter F defined as $\Sigma(\chi_{exptl}\text{-}\chi_{calc})^2$. *F'* is defined as $F' = F^2 / \nu$, where $\nu = N_{IDP} - \rho$. N_{IDP} is the number of independent data points, while ρ is the number of floated variables in each optimization step. *F'* is a measure of whether an added shell significantly improves the fit.

Table S3. EXAFS fits for $[Fe^{III}(TMC)(\eta^1\text{-}OOH)]^{2+}$ (**2**).[a]

	Fe–N/O			Fe–N/O			Fe•••C				
fit	*n*	*r*	σ^2	*n*	*r*	σ^2	*n*	*r*	σ^2	*F* [b]	*F'* [b]
1	5	2.17	5.2							127.5	848.2
2	6	2.17	7.3							156.0	1270
3	4	2.16	2.8	1	1.93	4.9				93.4	508.1
4	5	2.15	4.3	1	1.91	3.3				96.4	541.3
5	5	2.15	3.7	2	1.92	8.6				104.6	637.4
6	4	2.16	2.6	2	1.94	10.6				98. 7	567.2
7	4	2.15	2.7	1	1.93	4.5	3	2.91	4.8	24.18	44.41
							3	3.50	4.1		
8	5	2.15	4.3	1	1.91	2.9	3	2.91	4.5	28.61	62.17
							3	3.50	4.1		
9	**4**	**2.15**	**2.9**	**1**	**1.92**	**5.5**	**3**	**2.92**	**3.0**	**14.92**	**19.94**
							3	**3.52**	**4.0**		
							2	**3.13**	**1.0**		
10	5	2.15	4.6	1	1.90	3.2	3	2.92	2.6	17.78	28.31
							3	3.52	3.7		
							2	3.13	0.6		

[a] Fourier transform range $k = 2.0 – 14.0$ Å^{-1} (resolution = 0.13 Å). *r* is in units of Å; σ^2 is in units of 10^{-3} Å^2. All fits shown here were to Fourier-filtered data employing a back transformation range of 0.3-3.2 Å. Bolded fit parameters represent the best fit.

[b] Goodness-of-fit parameter F defined as $\Sigma(\chi_{exptl}\text{-}\chi_{calc})^2$. *F'* is defined as $F' = F^2 / \nu$, where $\nu = N_{IDP} – \rho$. N_{IDP} is the number of independent data points, while ρ is the number of floated variables in each optimization step. *F'* is a measure of whether an added shell significantly improves the fit.

Table S4. Vibrational frequencies of high-spin iron(III)-peroxo species.

	ν(Fe–O), cm^{-1} ($\Delta^{18}O$) [$\Delta^{2}H$]	ν(Fe–O), cm^{-1} ($\Delta^{18}O$) [$\Delta^{2}H$]	ref
Monoiron(III)-η^1-hydroperoxo			
2	676 (-24) [-1]	870 (-50) [-1]	[a]
$[Fe(H_2bppa)(OOH)]^{2+}$	621 (-22)	830 (-17) [-4]	10
E114A SOR	567 (-4)[b]	838 (-23)[b]	11
oxyhemerythrin	503 (-24) [-3]	844 (-48) [+4]	12
$[Fe(cyclam\text{-}PrS)(OOH)]^{+}$	419 (-19)	891 (-35) [c]	13
Monoiron(III)-η^1-alkylperoxo			
$[Fe(6\text{-}Me_3\text{-}TPA)(OO^tBu)]^{2+}$	637 (-25)	860[d]	14
$[Fe(H_2bppa)(OO^tBu)]^{2+}$	629	873/838	15
$[Fe(Tp)(OO^tBu)]^{+}$	625 (-42)	860[d]	16
$[Fe(15\text{-}TMC)(OTf)(OO^tBu)]^{+}$	612 (-21)	871 (-49)	17
$[Fe(15\text{-}TMC)(SPh)(OO^tBu)]^{+}$	584 (-19)	872 (-57)	17
Monoiron(III)-η^2-peroxo			
1	493 (-15)	826 (-41)	[a]
$[Fe(N4Py)(\eta^2\text{–}O_2)]^{+}$	495 (-17)	827 (-47)	18
$[Fe(tmpIm)(\eta^2\text{–}O_2)]^{-}$	475 (-20)	807 (-49)	19
E47A SOR	438 (-23)	850 (-48)	20

[a] this work; [b] data obtained in crystallo; [c] Fermi doublet observed to collapse in deuterated solvent but no isotopic shift reported; [d] data from -OOtBu-d9 complex; H_2bppa = bis(6-pivalamido-2-pyridylmethyl)(2-pyridylmethyl)amine; SOR = superoxide reductase; cyclam-PrS-H = 1-(3'-mercaptopropyl)-1,4,8,11-tetraazacyclotetradecane; 6-Me_3-TPA = tris(6-methyl-2-pyridylmethyl)amine; Tp = hydrotris(3-*tert*-butyl-5-isopropyl-1-pyrazolyl)borate; 15-TMC = 1,4,8,12-tetramethyl-1,4,8,12-tetraazacyclo-pentadecane; N4Py = N,N-bis(2-pyridylmethyl)-N-bis(2-pyridyl)methylamine; tmpIm = 5,10,15-tris(2',4',6'-trimethylphenyl)-20-(2'-(3"-imidazolylmethyl)-benzamido)phenyl)porphyrinate dianion.

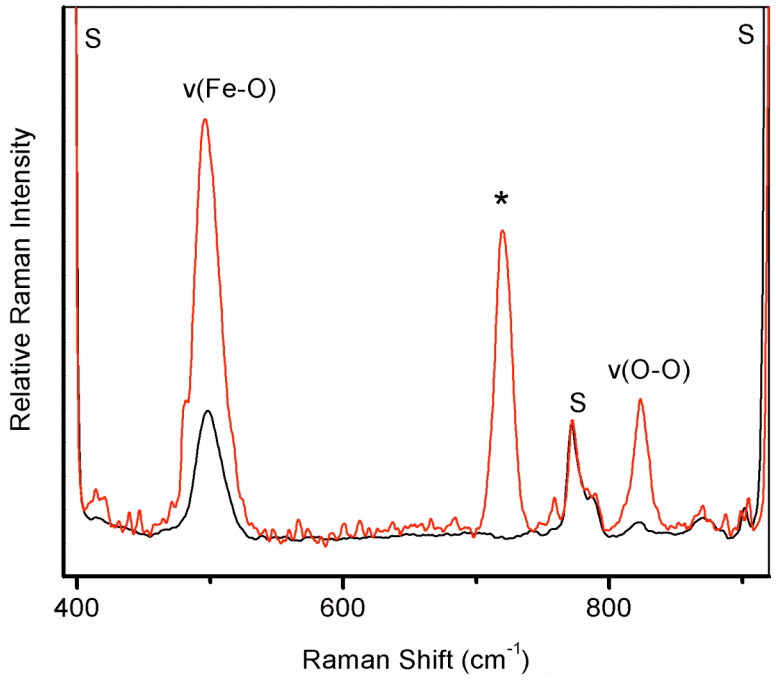

Figure S10. The resonance Raman spectra of **1** obtained with λ_{ex} = 647.1 nm (red) and 514.5 nm (black). "S" indicates peaks derived from CH_3CN solvent; asterisk denotes peaks derived from 647.1 nm notch filter. The spectra have been normalized according the 773 cm^{-1} peak of CH_3CN.

Due to the very low intensity of the peaks belonging to *ν*(Fe–O) and *ν*(O–O) of **2** (relative to the solvent peak) and the high susceptibility to photobleaching of the sample, we could not acquire very good data for both 647 nm and 514 nm laser line on the same frozen sample; the transient nature of the hydroperoxo in solution precluded comparisons between different frozen solution samples.

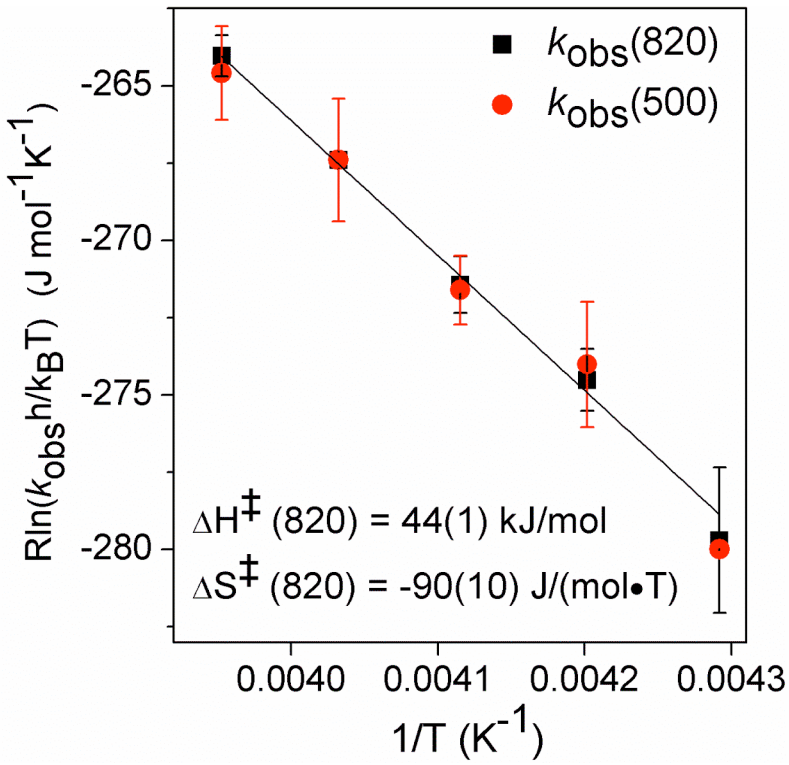

Figure S11. Eyring plot for the conversion of **2** to **3**. Experimental conditions: 1.5 mM **2**, 34 mM $HClO_4$, in CH_3CN; k_{obs} values were measured over the range of –40 °C to –20 °C. The black line is a linear fit for values of k_{obs}(820).

References:

1. Rohde, J.-U.; In, J.-H.; Lim, M. H.; Brennessel, W. W.; Bukowski, M. R.; Stubna, A.; Münck, E.; Nam, W.; Que, L., Jr. *Science* **2003**, *299*, 1037–1039.

2. (a) Stephenson, N. A.; Bell, A. T. *Anal. Bioanal. Chem.* **2005**, 381, 1289−1293. (b) Stephenson, N. A.; Bell, A. T. *J. Am. Chem. Soc.* **2005**, *127*, 8635–8643.

3. Münck, E.; Groves, J. L.; Tumolillo, T. A.; Debrunner, P. G. *Comput. Phys. Commun.* **1973**, *5*, 225–238.

4. England, J.; Martinho, M.; Farquhar, E.; Frisch, J.; Bominaar, E.; Münck, E.; Que, L. Jr. *Angew. Chem., Int. Ed.* **2009**, *48*, 3622–3626.

5. George, G. N. *EXAFSPAK*; Stanford Synchrotron Radiation Laboratory, Stanford Linear Accelerator Center: Stanford, CA, 2000.

6. Ankudinov, A. L.; Ravel, B.; Rehr, J. J.; Conradson, S. D. *Phys. Rev. B: Condens. Matter Mater. Phys.* **1998**, *58*, 7565–7576

7. Riggs-Gelasco, P. J.; Stemmler, T. L.; Penner-Hahn, J. E. *Coord. Chem. Rev.* **1995**, *144*, 245–286.

8. Wickman H. H.; Klein, M. P; Shirley, D. A. *Phys. Rev.* **1966**, *152*, 345–357.

9. Schmidt, M; Scherk, C; Iakovleva, O.; Nolting, H. F.; Meier, B.; Parak, F. *Inorg. Chim. Acta.* **1998**, *275*, 65–72.

10. Wada, A.; Ogo, S.; Nagatomo, S.; Kitagawa, T.; Watanabe, Y.; Jitsukawa, K.; Masuda, H. *Inorg. Chem.* **2002**, *41*, 616–618.

11. Katona, G.; Carpentier, P.; Nivière, V.; Amara, P.; Adam, V.; Ohana, J.; Tsanov, N.; Bourgeois, D. *Science* **2007**, *316*, 449–453.

12. Shiemke, A. J.; Loehr, T. M.; Sanders-Loehr, J. *J. Am. Chem. Soc.* **1984,** *106*, 4951–4956.

13. Kitagawa, T.; Dey, A.; Lugo-Mas, P.; Benedict, J. B.; Kaminsky, W.; Solomon, E.; Kovacs, J. A. *J. Am. Chem. Soc.* **2006**, *128*, 14448–14449.

14. Zang, Y.; Kim, J.; Dong, Y.; Wilkinson, E. C.; Appelman, E. H.; Que, L., Jr. *J. Am. Chem. Soc.* **1997**, *119*, 4197–4205.

15. Wada, A.; Ogo, S.; Watanabe, Y.; Mukai, M.; Kitagawa, T.; Jitsukawa, K.; Masuda, H.; Einaga, H. *Inorg. Chem.* **1999**, *38*, 3592–3593.

16. Lehnert, N.; Fujisawa, K.; Solomon, E. I. *Inorg. Chem.* **2003**, *42*, 469–481.

17. Namuswe, F.; Hayashi, T.; Jiang, Y.; Kasper, G. D.; Sarjeant, A. A. N.; Moënne-Loccoz, P.; Goldberg, D. P. *J. Am. Chem. Soc.* **2009**, *132*, 157–167.

18. Roelfes, G.; Vrajmasu, V.; Chen, K.; Ho, R. Y. N.; Rohde, J.-U.; Zondervan, C.; la Crois, R. M.; Schudde, E. P.; Lutz, M.; Spek, A. L.; Hage, R.; Feringa, B. L.; Münck, E.; Que, L., Jr. *Inorg. Chem.* **2003**, *42*, 2639–2653.

19. Liu, J.-G.; Ohta, T.; Yamaguchi, S.; Ogura, T.; Sakamoto, S.; Maeda, Y.; Naruta, Y. *Angew. Chem., Int. Ed.* **2009**, *48*, 9262–9267.

20. Mathé, C.; Mattioli, T. A.; Horner, O.; Lombard, M.; Latour, J.-M.; Fontecave, M.; Nivière, V. *J. Am. Chem. Soc.* **2002**, *124*, 4966–4967.